Article

Assessment of Flood-Induced Geomorphic Changes in Sidere Creek of the Mountainous Basin Using Small UAV-Based Imagery

Mehmet Yavuz * and Mustafa Tufekcioglu

Department of Forest Engineering, Faculty of Forestry, Artvin Coruh University, 08100 Artvin, Türkiye; mtufekcioglu61@artvin.edu.tr
* Correspondence: myavuz@artvin.edu.tr

Abstract: Floods often cause changes in the hydro-geomorphology of riverbeds and banks. These changes need to be closely monitored to find a balance and exchange between lateral and vertical erosion and deposition, upstream local sediment supply, and a stream's transport capacity. Low-frequency cross-sectional field surveys cannot map hard-to-reach locations. Innovative techniques, such as small unmanned aerial vehicles (UAVs), must be employed to monitor these processes. This research compared historical data with a UAV survey and the Pix4DMapper structure-from-motion (SfM) program to assess the longitudinal, lateral, and vertical changes of Sidere Creek in the eastern Black Sea, Türkiye. Digitization was undertaken using 2011–2015–2017 Google Earth photographs, 1960s topographic maps, and 2023 orthomosaics. ArcGIS 10.6 was used to delineate the centerlines (thalweg), left/right banks, alluvial bars, active channel widths, and channel confinement layers. Channel Migration Toolbox and CloudCompare were utilized for analyzing lateral and vertical morphological changes, respectively. The active channel migrated 25.57 m during 1960–2011, 15.84 m during 2011–2015, 6.96 m during 2015–2017, and 5.79 m during 2017–2023. Left-bank channel confinement rose from 2.4% to 42% and right-bank channel confinement from 5.9% to 34.8% over 63 years. Neither stream meandering nor sinuosity index changed statistically. Active channel boundary widths varied from 149.79 m to 9.46 m, averaging 37.3 m. It can be concluded that UAV surveys can precisely measure and monitor the stream channel longitudinal, lateral, and vertical morphological changes at a lower cost and in less time than previous methods.

Keywords: longitudinal profiling; stream lateral morphological changes; small UAVs

1. Introduction

Streams are complex and dynamic conductors for energy and sediment transfer downstream that cause subsequent morphologic, hydrological, and biological changes in the riverscapes as a result of the variation in the hydrologic regime of the basin. Streams are an essential component of the Earth's topography. The loss of riparian vegetation, channel straightening, channel narrowing, the construction of dams and small hydroelectric power plants, and earthworks like quarrying are all caused by the increased stream power itself [1–4]. All these factors can further propagate the imbalance between the supply of sediment sources by erosion and the volume of stream water that is intended to carry it within the fluvial system [5,6].

On the other hand, for a long time, soil erosion with the associated sedimentation in surface water has been one of the main concerns for researchers, not only from a water quality perspective but also for the aquatic life living in the respective environment. The erosion/deposition processes in stream channels and their floodplains are significantly affected by high stream stages and/or flash floods that cause major changes in the stream bed, banks, width and longitudinal aspects, and adjacent corridors within the riparian

zone [7–10]. Most of the hydro-morphological changes in the riverscapes usually take place during the high stages of floods [5,11], where the sedimentary characteristics of the stream bed and the pattern of flood events [12] also damage aquatic habitats [13], agricultural areas, and residential areas [14].

Floods cause channels and floodplains to react in intricate and interactive ways that involve lateral and vertical erosion and deposition. The hydraulic erosivity of the flood event, the erodibility of the floodplain, the channel along valley edges, and the equilibrium between "upstream local sediment supply" and "stream's transport capacity" all must be closely monitored to mediate these processes [14]. According to Nanson and Croke [15], flood erosivity is a function of the discharge volume, channel and valley slopes, and the channel's confinement by the valley edges. In addition, a stream's debris loads are influenced by sediments from landslides, both shallow and deep, and debris from surface water erosion of the surrounding terrain [16–18]. The findings of Lauer et al. [19] regarding a Minnesota river basin showed that the size distribution of sediment eroded from the banks and the deposits of bars both affect the size distribution of any material discharged downstream.

Alterations of the morphological features of the mountainous river channel on spatial and temporal scales due to floods can be an indicator of channel disequilibrium [9]. Therefore, the continuous monitoring of the physical and hydrological conditions of the riverscapes is an important step for identifying and analyzing the key elements of controlling factors of the channel response and habitat quality [20–22].

Despite the use of hybrid methodologies and techniques, estimating riverbank erosion/deposition and shifting rates, as well as their expected future positions [8,23], are difficult tasks. The majority of approaches rely on substantial field-based spatiotemporal monitoring [24] or known hydrologic models [25]. Based on multi-temporal geomorphological data, a variety of methodologies for evaluating the pace of riverbank erosion [26] and future prediction of positional shifting [27] have been developed (long, intermediate, and short term) [28]. For instance, Lallias-Tacon et al. [29] linked the construction of floodplains with the characteristics of vegetation patches in the Drôme, Bès, and Bouinenc River catchments in Lyon, southeast France, by combining airborne light detection and ranging (LiDAR) data with old aerial photographs. They came to the conclusion that shrubby patches were a reliable indicator for retracing the chronology of incision periods. Dewan et al. [30], on the other hand, evaluated the channel features of the Ganges (regulated) and Padma (unregulated) Rivers in Bangladesh, utilizing 38 years of data and multi-temporal Landsat imagery. They discovered that the conventional meander theory is in conflict with the relationship between bank curvature and river erosion and accretion. Abate et al. [31] used SPOT images from 2006 and two historic aerial photos from 1957 and 1980 to examine the morphological changes of the Gumara River channel over 50 years in Ethiopia's upper Blue Nile basin. They discovered that sediment buildup caused by land degradation and direct intervention on river banks caused a backwater effect because of artificially elevated lake levels. According to Bao et al. [32], a significant landslide in Jinsha River, China, obstructed the river and caused a 120 m tall wave to go in the opposite direction of the riverbank flow, raising the water level by 120 m. Lauer et al. [19] used aerial photographs to measure the channel width at 16 multi-bend subreaches for the years 1938 to 2015 by digitizing the space between vegetation lines and dividing by the centerline length. They discovered that widening was connected to "lateral centerline movement" and "temporal change in at-a-station" hydraulic geometry for "water surface width", indicating that it is linked to cross-sectional change rather than just upward movement of the vegetation line. With a recent improvement in innovative technologies, unmanned aerial vehicles (UAVs) became popular application tools for remote monitoring, assessing, and mapping the environment in much more detail [18,33,34]. As tools to assess and manage soil and water resources, the utilization of UAVs has found its place in many different fields of environmental study, such as floods, landslides, stream morphology and restoration, stream thermal condition, intertidal

mudflat mapping, bed load transport, sand and gravel mining, and earthwork projects [13,22,33–40]. Some traditional streambank erosion evaluation techniques reported by researchers are the mixture of channel chains, the Rivermorph program, erosion pins, the BANCS procedures developed by Rosgen [41], sedimentological evidence, botanical evidence, historical sources, planimetric resurveys, repeated cross-section profiling, and "terrestrial photogrammetry" [42–44].

As an alternative to conventional remote sensing monitoring techniques, cross-sectional field resurveys, and erosion pins in stream channel assessment, recent advancements in innovative modern techniques, such as the conventional GPS (GNSS-enabled) surveying, terrestrial laser scanning (TLS), and airborne LiDAR surveying, have surpassed the quality and quantity of traditional surveying techniques. But these technologies lack the ability to reduce the cost and time required to acquire such a detailed survey. The structure-from-motion (SfM) techniques from the unmanned aerial vehicle (UAV) images, on the other hand, offer the same level of accuracy that the LiDAR provides at a lower cost and can be used more frequently, at any time of day, and in any season, with a little investment [43–45]. UAVs offer the advantage of providing accurate monitoring with high spatial and multi-temporal resolutions for evaluating the pace of the streambank bed erosion/deposition, future prediction of positional shifting [18,37,43–45], mapping hard-to-reach locations with high survey frequency [34,36], and producing detailed geomorphic and habitat maps at substantially low costs and time [33,36,38]. The main limitations of using UAVs are extreme weather conditions due to safety reasons and battery limitations on the flight time [46]. Due to the capacity for producing very high-resolution 3D models, as demonstrated by Junaid et al. [34] for rock stability studies and Yavuz et al. [18] for streamside landslides, the survey capacity of small UAVs on lateral and vertical morphological changes on a stream reach scale has not yet been fully examined.

The purpose of this study was to evaluate geomorphological changes from 1960 to 2023 using small unmanned aerial vehicles (sUAVs) in Senkoy Reach of Sidere Creek in Arhavi River Watershed, Arhavi, Türkiye, including longitudinal profiles, stream bed slope, meandering, and sinuosity; lateral channel migration on the thalweg line; channel width; the number of pools and riffles; and vertical movement of the stream channel. The stream channel bed, bank heights, and floodplain terraces are among the vertical morphological changes that involve incision and deposition. The effectiveness of the small UAV survey in stream bed monitoring was assessed using their multi-temporal resolution and ability to penetrate woody stream channels.

2. Materials and Methods

2.1. The Case Study Site of Senkoy Reach

The Senkoy Reach case study site was located within the Arhavi River Watershed's boundary in Arhavi Province, Türkiye, and is situated between the 41.320372° and 41.309296° N latitude and the 41.315607° and 41.348144° E longitude geographic coordinates. Senkoy Reach is 2785 m long with an elevation range from 20 to 157 m at mean sea level (MSL). Most of the research area had a slope of less than 8%, while some locations had a flat slope grade.

The Balikli sub-watershed, which is located in the eastern half of the Arhavi River Watershed, supplies the water flow of Senkoy Reach by bringing all of the sediments into Sidere Creek before it merges with Kapistre Creek. Senkoy Reach's drainage area covers 657.24 hectares, most of which is an urbanized area. The vast majority of the arable agricultural lands in the Balikli sub-watershed are tea and hazelnut orchards. The remaining cultivated areas are used for corn, fruit, and vegetable growing. The areas that are forested are located at high elevated lands within the subwatershed. The riparian zone of Senkoy Reach consists of hazelnut trees, shrubs, and alder trees. The oriental persimmon trees can also be seen along the stream in shrub and tree forms.

Senkoy Reach was chosen to represent the lowland part of the Arhavi River Watershed (Figure 1). Senkoy Reach is located at the merging point of Sidere Creek and Kapistre Creek, where the slopes of both rivers start flattening before reaching the Black Sea (Figure 1).
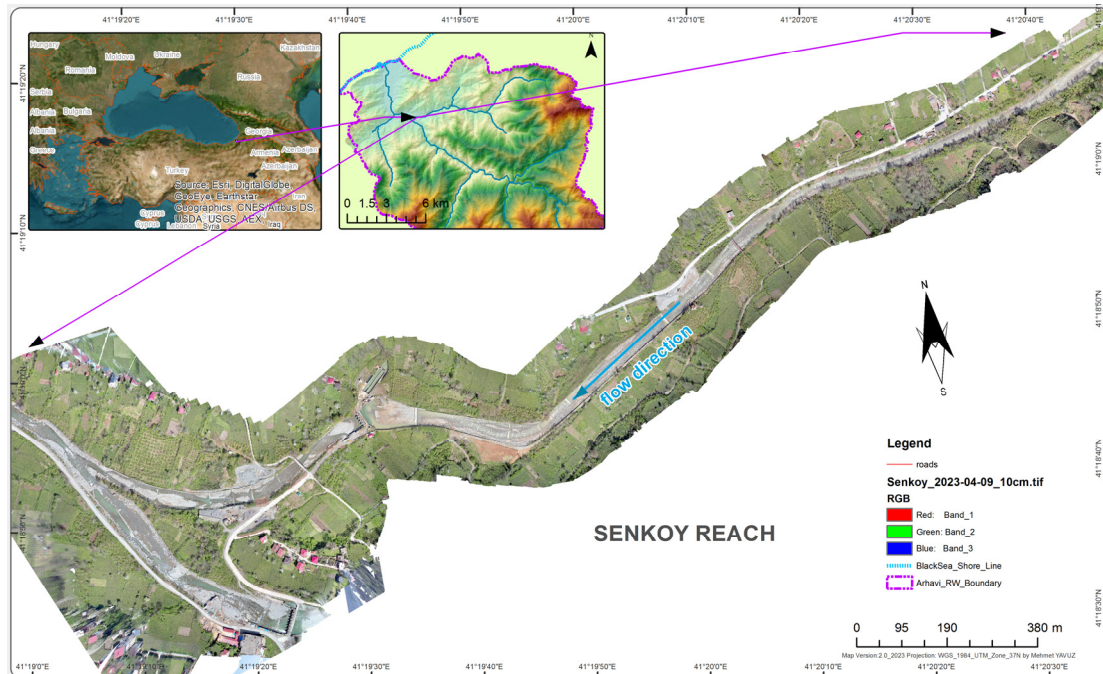

Figure 1. The location of the Senkoy Village Reach site within the Arhavi River Watershed (Türkiye).

2.2. Linear Stream Channel Surveying with a UAV

The field surveys in the study area were conducted on 21 September 2021 and 9 April 2023 using the "DJI Matrice 300 RTK (M300) Enterprise" drone (DJI, Shenzhen, China). The M300 has a built-in RTK capable of centimeter-level horizontal and vertical accuracy. The stream reaches were recorded on both occasions using the DJI's proprietary capture tool, namely, the Pilot2 app. The flight path was set to be along the stream course with a 100 m swath width on both sides of the stream centerlines. The flight altitude was set to 104 m and the forward overlap of the photos was set at 80% along the stream course (Table 1). The resolution of each photo captured was 4056 × 3040 pixels. The thermal photo resolution was 512 × 548 pixels.

The fall and early spring seasons were chosen as the photo collection period due to the stream flow in the stream course being the lowest (3–15 cm in the stream bed area). This allowed the photogrammetric process to see the streambed features and would enable capturing the boulders, cobbles, and gravel. The shallow and clear water allowed for mapping the streambed altitude and topography by identifying the keypoint stream features for the photogrammetric matching process. According to the other studies [47–50], photos acquired via UAV-based surveying are suitable and allow for mapping optical bathymetric modeling of the study's submerged area for DTM generation [51].

Table 1. Characteristics of the UAV surveys taken by flying over Senkoy Reach in Türkiye.

Site Name	Image Date	UAV	Flight Height (m)	Area Covered (km²)	Strips	Over-Lap (%)	Side-Lap (%)	UAV Image Footprint on Ground (m)	Number of Images
Senkoy, TR	21 September 2021	DJI Matrice 300 RTK	50	0.025	3	80	70	123 × 92	25
Senkoy, TR	8 April 2023	DJI Matrice 300 RTK	104	0.957	3	80	70	255 × 191	752

Any spatial uncertainty associated with digitizing errors due to delineating channel centerlines and banks was resolved with a trained remote sensing expert (the first author of this study). All centerlines and banks were delineated with only the same expert. The geometric errors related to image co-registration among a 1960 topo map; 2011, 2015, 2017 GE imagery; and 2023 orthomosaic imagery were corrected using the root square mean error (RMSE) technique [52–54]. A network of 22 ground control points (GCPs) was established throughout the stream corridor to co-register and georeference the images. House corners and road bridge cross-sections that could be seen on the 1960 topo map and photos from 2011 to 2015 to 2017 to 2023 were chosen as GCPs. An RMSE of less than 50% of the pixel length and the second-order polynomial transformation were applied during georeferencing [52,55]. The horizontal (XY) and vertical (Z) geolocational accuracies of the 2021 and 2023 ortho-images were obtained from the quality report during the photogrammetric process with Pix4DMapper (ver. 4.5.6) software (Table 2). Because the DJI M300 RTK has its own built-in RTK, no additional GCPs were used during the photogrammetric process.

Table 2. The horizontal (XY) and vertical (Z) geolocational RMSE errors generated during the photogrammetric process with Pix4DMapper software.

Site Name	Image Date	Software	GPS-GNSS Receiver	GCPs	Orthophoto Resolution (cm/pix)	XY RMSE (m)	Z RMSE (m)
Senkoy, TR	21 September 2021	Pix4D ver. 4.5.6	Built-in RTK	Built-in RTK	1.00	0.358	0.414
Senkoy, TR	9 April 2023	Pix4D ver. 4.5.6	Built-in RTK	Built-in RTK	3.08	1.182	1.392

2.3. Channel Centerline and Active Channel Boundary Mapping

The channel centerlines were digitized manually from the aerial imagery obtained from sUAV, Google Earth, and historical topographic maps. For the mitigation analysis, the centerline of the wetted base-flow channel was used (Figure 2). In order to estimate the channel bed erosion, the centerlines were delineated at the deepest flow areas (thalweg line). Also, the active channel borders, which are defined by the wetted base flow and exposed gravel bars next to the wet channel [56], were delineated.

Figure 2. The stream channel centerline (magenta) and cross-section lines (blue) that were used for channel migration analysis from 2015 to 2017 for the Senkoy Village Reach site within the Arhavi River Watershed (Türkiye).

The gravel bars were mapped using the SegmentMeanShift (SMS) algorithm within the ArcGIS 10.6 software (ESRI, Redlands, CA, USA) and then vectorized using the ArcScan extension. Red, green, and blue bands from the orthophotos served as the input layers for this SMS analysis. During the SMS process, each input band was given an equal degree of weighting [57]. The initial parameters for the SMS were set to a spectral detail of 15.5, a minimum segment size in pixels of 20, and a spatial detail of 15. These values were chosen to automatically group adjacent pixels with comparable spectral and spatial properties together, thereby identifying feature segments in the orthophotos of the study reach. Any paved roads that showed similar spectral characteristics were excluded from the active channel boundaries. The tops of the levees that were 50 cm wide were included as a confined boundary. The flow chart of the methodological process can be seen in Figure 3.
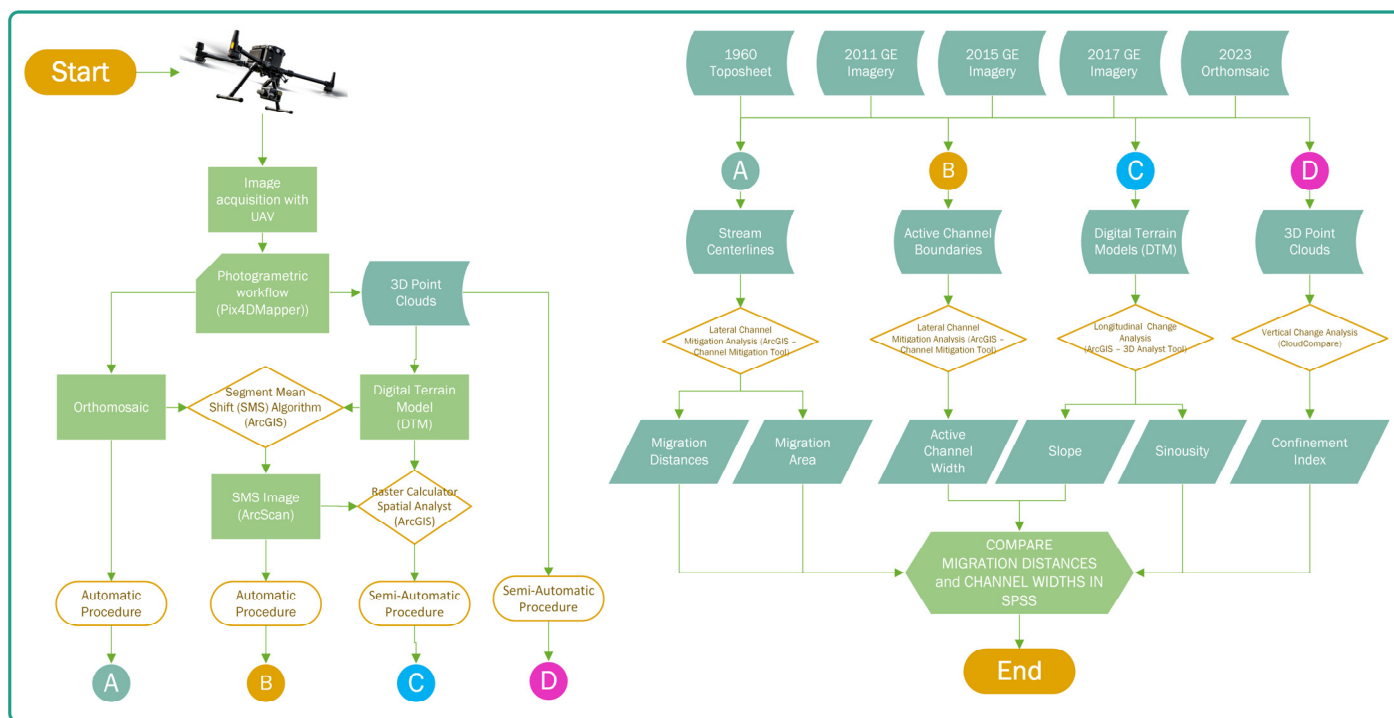

Figure 3. The flow chart of the methodologies used in this study.

2.4. Channel Longitudinal Profiles, Meander Amplitude, and Confinement Index

The meander amplitude (sinuosity index) was calculated using the centerline length divided by the straight-line length from the start to end points of the centerline. A sinuosity index value equal to 1 indicates no meandering. If the sinuosity index becomes larger than one, then the stream meanders more.

The channel confinements were divided into three categories: (1) unconfined, (2) natural confinement, and (3) man-made confinements. The confinement codes were assigned as 2 for natural confinement, 1 for man-made confinement, and 0 for unconfined channel boundaries. For calculating the confinement index for each year's channel boundaries, total confinement lengths were divided by the channel lengths for the left and right banks separately. Another channel confinement method developed by Wohl [58] and Sholtes et al. [14] uses the ratio of the channel reach's bottom width to the top-of-bank width. The first method was adopted due to the ability to assess the left and right banks separately.

The Digital Terrain Model (DTM) layer for 1960 was created with the TopotoDEM tool in ArcGIS 10.6 using 10 m counter lines in the 1960 toposheets. The 12.5 m resolution ALOS PALSAR RTC data from Alaska Satellite Facility, USA, was used to create longitudinal profiles for 2011, 2015, and 2017 channel centerlines. The ALOS PALSAR data were radiometrically and geometrically corrected data products obtained from the synthetic aperture radar (SAR) satellites and Shuttle Radar Topographic Mission (SRTM) data [59,60]. The digital terrain model (DTM) generated from the structure-from-motion UAV imagery was used for longitudinal profiling of the 2023 channel centerline. The orthometric height of the 2023 DTM data created with EGM96 vertical datum. The DTM data was converted to ellipsoid heights using GeoidEval (version 2.2) online utility [61]. The GeoidEval uses interpolation in a "grid of values for the earth gravity models" EGM84, EGM96, or EGM2008 to calculate the height of the geoid above the WGS84 ellipsoid. The latitude and longitude coordinates of the vertices on each stream channel centerline were converted to ellipsoidal heights using this tool. In order to calculate the percent slope for each channel centerline, the shape files were converted to route lines and then 3D lines using the ArcGIS Linear Referencing Tool and 3D Analyst Tool (ESRI, Redlands, CA, USA). During the conversion, the *route identifier field* was set to "TRANSECT_ID", the *measure source* was set to "LENGTH", and the *coordinate priority* was set to "UPPER LEFT". The elevation properties were added to the Z feature of the feature class and Z values were updated with the digital terrain model (DTM) layer. Then, the longitudinal profiles were created for each channel centerlines. The average slope, slope gain, and slope loss were calculated using these profiles. The WGS 1984 UTM Zone 37 was chosen as the XY coordinate system for all layers.

2.5. Reach-Average Channel Migration, Total Channel Migration Distances, and Active Channel Widths

In order to calculate the total lateral migration distances and channel widths, the Channel Migration Toolbox extension [62–65] was employed within the ArcGIS 10.6 environment. According to Hooke [66], channel migration is quantified as a lateral shift in the channel centerlines. The tool uses stream centerlines and cross-section transects along each stream to measure active channel widening and the migration rate. Channel migration rates fluctuate along channel meanders [15,67,68]; hence, it is important to capture variability inside meander bends by spacing cross-section transects closer together than a typical meander wavelength. The meander wavelengths in our study area ranged from 100 m to 700 m. For that reason, we chose 100 m, i.e., the lowest space distance between each cross-section transect. Using the Channel Migration Toolbox sub-tools, the (1) reach-average channel migration rate, (2) transect generation, (3) transect channel migration, and (4) transect channel widths were all calculated. The main sources of input layers were the channel centerlines (sub-tools 1 and 3) and the channel outlines that were

digitally reconstructed from historic topographic maps and aerial photos (sub-tool 4). Sub-tool 2 was used for transect generation.

The reach-average channel migration rate was calculated by dividing the migration area by the reach length as defined by Hooke [66] (Equation (1)):

$$\text{reach} - \text{average channel migration rate} = \frac{\text{migration area}}{\text{reach length}} \tag{1}$$

2.6. Mapping Degradation and Aggradation Patterns

The reach channels are actively deposited by aggregating their beds. Aggregation helps channel migration by promoting the deposition of sediments and the creation of bars that divert the stream channel [69]. The erosion and deposition within the reach corridor were estimated using the DEMs-of-differences (DoDs) measured from the 5 cm resolution DTMs generated from the SfM data collected using the DJI Matrice 300 RTK drone. The drones were flown when the stream was in a low base flow condition.

2.7. Vertical Morphological Change Analysis

The vertical geomorphological change analysis was conducted on the 3D point clouds using free public CloudCompare (ver. 2.13) software [70]. The stream bottom profiles, bank heights, and bank angles were measured. Only the active channel bottoms and channel centerlines are reported in this paper. The 3D point clouds were used for point-to-point comparisons between the 21 September 2021 and 8 April 2023 UAV flights. The conditions of the concrete and dry walls as confinements were also evaluated during the analysis.

2.8. Vegetation Analysis

The vegetation in the riparian areas was analyzed in order to measure the percent vegetation cover and number of tree species present around the stream reaches. Data for the historical vegetation along the riparian buffer were collected from CORINE 2018 database, forest management maps, and the maps obtained via the UAV imagery from this study.

2.9. Sensitivity Analysis of the Spacing of Cross-Sections

The locations of the cross-section transects along a river system are important and usually differ according to the purpose of the project goals [71,72]. According to Samuels [71], the space between transects should not be more than 10 to 20 times the width of a bankfull. Regardless of river size, Glenn et al. [73] advised using transect spacings of 0.4 and 0.8 of the bankfull width for simple and complex rivers, respectively.

The sensitivity analysis was used to assess how measurements of channel migration distance were affected by the distance between each cross-section. The analysis was conducted by using cross-section spacings of 10, 25, 50, 75, 100, 150, and 200 m. The results were compared with the measurements obtained from the UAV survey using the one-way ANOVA test in the IBM SPSS 19 statistical program (IBM Corp., Armonk, NY, USA). The channel migration distances were set as the dependent variable, while the transect spacings were set as factors. The datasets were divided into four groups: 1960–2011, 2011–2015, 2015–2017, and 2017–2023. If the test was significant, the particular transect spacing was not provided in the ANOVA test results. To determine which transect spacing was different, Tukey's ad hoc test was used.

2.10. Field Ground-Truthing and Statistical Analysis

The cross-section transects generated by the Channel Mitigation Tool and the active channel widths were measured in the field for ground-truthing. A systematic sampling of 13 (transects 6, 8, 10, 13, 14, 15, 16, 17, 18, 21, 22, 23, and 27) of 27 cross-section transects with a random start were selected. The active channel widths were measured using the

TruPulse 360 laser rangefinder (Laser Technology, Inc., Centennial, CO, USA), which is capable of measuring the horizontal distance (HD), slope distance (SD), vertical distance (VD), inclination angles, and azimuth with target acquisition and increased accuracies on any level of 3D survey missions. The active channel width measurements were compared with the measurements made with UAV images using the pairwise comparison test. The variance of analysis (ANOVA) test was used to find the lateral and longitudinal changes from 1960 to 2023. All statistical analysis was performed using the IBM SPSS 19 statistical program (IBM Corp., Armonk, NY, USA).

3. Results

The active channel's lateral (width, centerlines (thalweg), and confinement index) and longitudinal changes (sinuosity index, channel mean, gain (increase), and loss (decrease) slopes) were calculated and the experimental results are summarized in the following subsections.

3.1. Channel Longitudinal Profiles, Meander Amplitudes, and Confinement Index Results

The longitudinal profiles of the stream centerlines for 2011, 2015, and 2017 are depicted in Figure 4a–c. These profiles show bumps and pits that are indications of incisions and aggregations along the stream channel bottom. Any slope incline or decline on these bumps and pits was measured and the average values are depicted in Table 3. The average slope between the start and end points of each stream centerline ranged from 2.4% to 7.7%. The confinement index results for 1960, 2011, 2015, 2017, and 2023 were 0.024, 0.011, 0.484, 0.481, and 0.420 for the left banks and 0.059, 0.129, 0.358, 0.396, and 0.348 right banks, respectively (Table 3). The average height of the walls used for confinement was 1.9 m on the channel right banks and 1.5 m on the channel left banks.
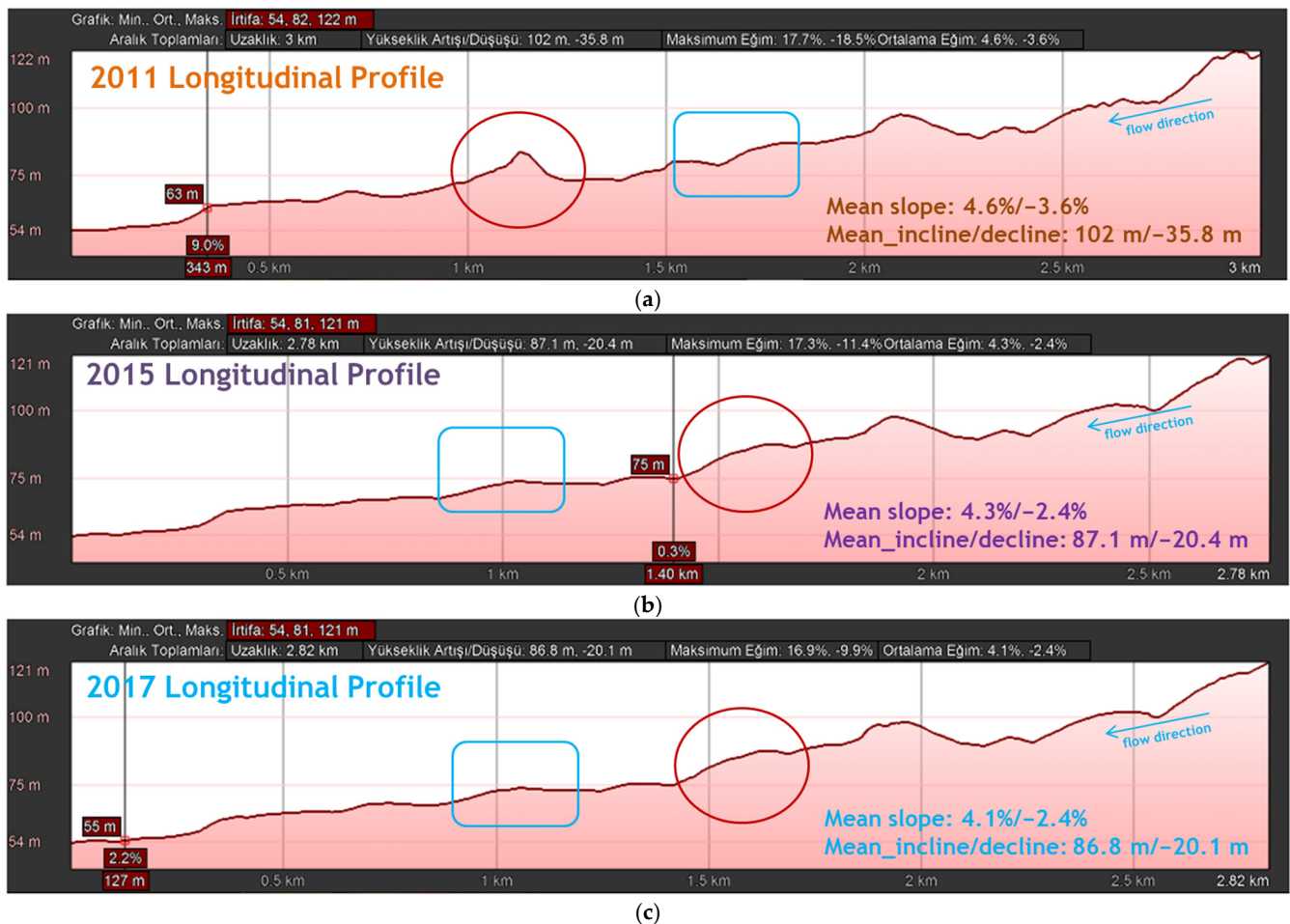

(a)

(b)

(c)

Figure 4. Longitudinal profiles of Senkoy Reach within the Arhavi River Watershed from (**a**) 2011, (**b**) 2015, and (**c**) 2017. The red circle indicates deposition and the blue rectangle indicates erosion on the stream bed.

The meandering and average sinuosity indices measured were 1.105, 1.210, 1.096, 1.123, and 1.111 for 1960, 2011, 2015, 2017, and 2023, respectively (Table 3).

Table 3. Results of the longitudinal channel profiles from 1960 to 2023 in Senkoy Reach, Arhavi, Türkiye. na: data is not available.
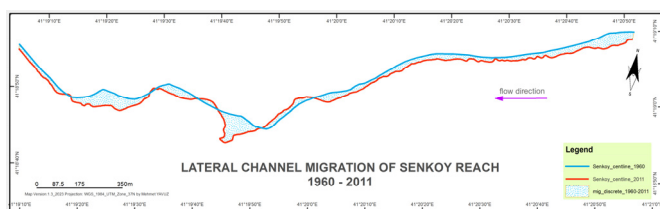
	1960	**2011**	**2015**	**2017**	**2023**
Gain average slope (%)	na	4.6	4.3	4.1	na
Loss average slope (%)	na	−3.6	−2.4	−2.4	na
Slope (%)	5.8	7.7	5.9	5.7	2.4
Mean incline (m)	na	102.0	87.1	86.8	na
Mean decline (m)	na	−35.8	−20.4	−20.1	na
Confinement index—left bank (LB_CI)	0.024	0.011	0.484	0.481	0.420
Confinement index—right bank (RB_CI)	0.059	0.129	0.358	0.396	0.348
Sinuosity index (SI)	1.105	1.210	1.096	1.123	1.111

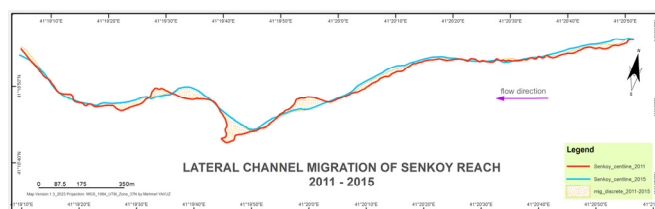*3.2. Reach-Average Channel Migration Rate Results*

The reach-average migration rates for 1960–2011, 2011–2015, 2015–2017, and 2017–2023 were found to be 24.06, 14.66, 6.70, and 6.07 m, respectively (Table 4). The most active period was 2011–2015, with a migration rate of 3.67 m/year. The least active period was 1960–2011, with a migration rate of 0.47 m/year. The resulting maps can be seen in Figure 5.

Table 4. Results of the reach-average channel migration rates for the periods 1960–2011, 2011–2015, 2015–2017, and 2017–2023.
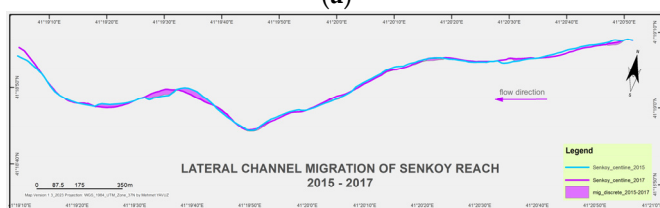
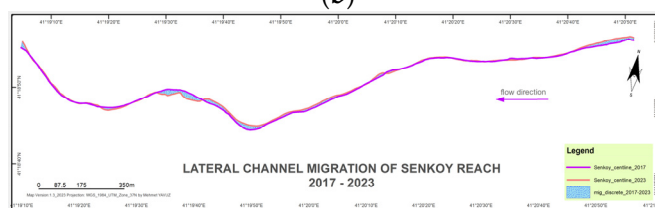| Migration Area	Beginning Year	End Year	Total Years	Reach-Average Migration Rate	Migration Rate
(m²)				(m)	(m/year)
66,961.0	1960	2011	51	24.06	0.47
40,803.7	2011	2015	4	14.66	3.67
18,632.7	2015	2017	2	6.70	3.35
16,895.8	2017	2023	6	6.07	1.01

(**a**)

(**b**)

(**c**)

(**d**)

Figure 5. Maps of the reach-average channel migration rates of Senkoy Reach within the Arhavi River Watershed for the periods (**a**) 1960–2011, (**b**) 2011–2015, (**c**) 2015–2017, and (**d**) 2017–2023. The shaded areas show the lateral channel migrated polygons for each period.

3.3. Total Channel Migration Distance Results

The channel migration distance measurements were taken for the equally spaced (100 m) 27 cross-sections. The descriptive summary statistics of the results of total channel migration distance from 1960 to 2023 are depicted in Table 5. The maximum migration distance was 116 m with an average of 25.57 m and took place from 1960 to 2011. The minimum migration distance was 0.00 m.

Table 5. Descriptive statistics of the lateral channel migration distances based on the cross-section transects from 1960 to 2023 in Senkoy Reach, Arhavi, Türkiye.

Period		N	Min	Max	Mean	SE	SD	VAR	Skewness	Skew SE	Kurtosis	Kurt SE
1960–2011	Migration Distance (m)	26	2	116	25.57	4.508	22.988	528.470	2.718	0.456	9.296	0.887
2011–2015		27	1	87	15.84	3.450	17.927	321.363	2.717	0.448	9.201	0.872
2015–2017		24	0	21	6.96	1.239	6.072	36.865	1.031	0.472	0.428	0.918
2017–2023		27	0	15	5.79	0.829	4.308	18.558	0.684	0.448	−0.669	0.872

In order to see the migration detail at each cross-section, the resulting measurements can be seen in Table 6 and Figure 6.
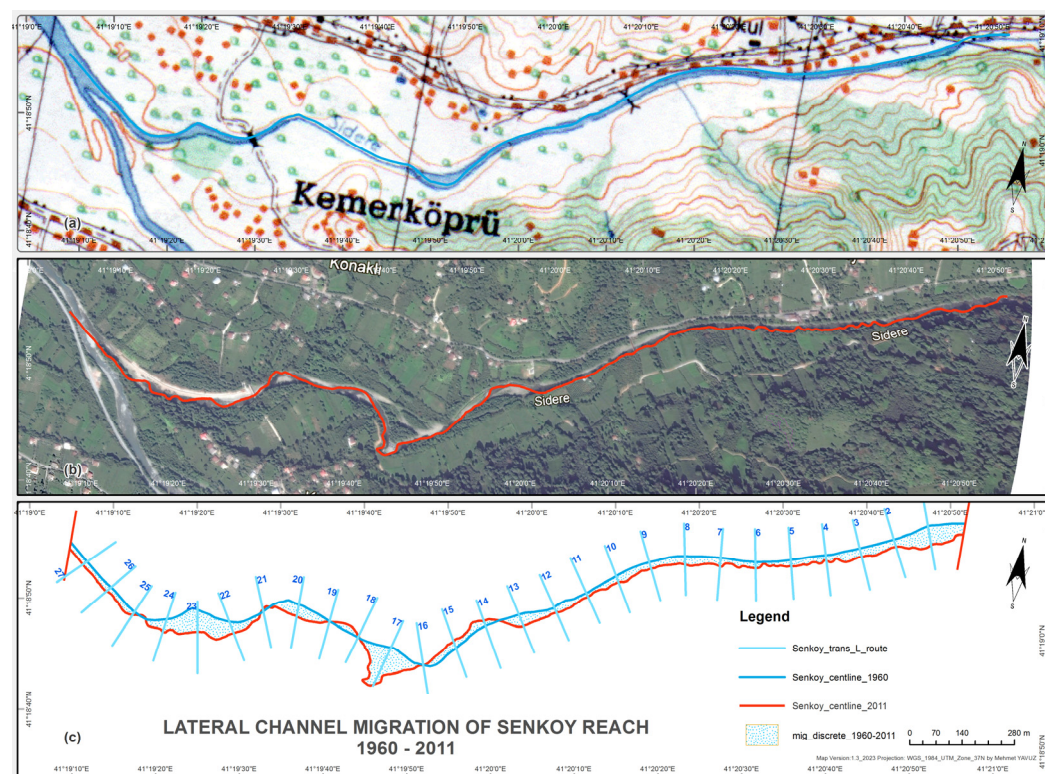

Figure 6. The lateral channel migration from 1960 (**a**) to 2011 (**b**) at the Senkoy Village Reach site within the Arhavi River Watershed (Türkiye). (**c**) The blue-shaded areas represent the discrete migration region from 1960 (blue) to 2011 (red) stream channel centerlines. The cross-section ID numbers increase along the flow direction. The 1960 topographical map is shown in (**a**), while the 2011 GE image is depicted in (**b**).

Table 6. Results of total channel migration distances from 1960 to 2023 based on the 27 cross-section measurements for Senkoy Reach in Arhavi, Türkiye. The red numbers show the maximum migration distances for each period.

Cross-Section ID	27	26	25	24	23	22	21	20	19	18	17	16	15	14	13	12	11	10	9	8	7	6	5	4	3	2	1
1960–2011	14.4	17.4	10.0	36.4	61.5	34.1	5.4	33.6	1.9	4.2	115.9	0.0	19.4	14.8	35.3	16.1	11.8	18.4	18.9	23.6	24.3	18.1	17.8	14.6	23.8	20.4	53.0
2011–2015	2.2	5.4	6.8	8.4	9.1	22.0	29.5	23.8	26.9	1.1	86.8	14.6	6.6	48.4	4.6	11.1	20.7	22.9	7.9	11.1	3.3	6.4	1.3	1.3	13.1	10.1	22.4
2015–2017	15.8	0.0	0.0	4.7	13.8	3.2	20.4	1.7	21.2	5.6	1.6	3.7	6.4	0.7	9.1	0.6	6.2	10.0	4.2	0.0	2.0	0.3	11.2	0.2	10.7	7.2	6.3
2017–2023	2.1	2.4	3.9	1.3	10.5	0.2	2.2	13.8	12.2	11.3	11.5	7.7	7.8	7.8	7.9	4.4	5.3	3.8	2.9	2.9	0.6	1.9	5.1	2.3	1.9	7.6	15.1

Total Migration Distance (m)

3.4. Total Channel Width Results

The active channel widths for each year were measured for the 27 cross-sections. The maximum channel width was found in 1960 at 149.79 m. The minimum channel width was found in 2011 at 9.46 m. Average-wise, the channel widths were 56.96, 32.96, 34.16, 30.14, and 32.27 m in 1960, 2011, 2015, 2017, and 2023, respectively (Table 7).

Table 7. Descriptive statistics of the active channel widths from 1960 to 2023 based on the 27 cross-section measurements for Senkoy Reach.

Year	N	Minimum	Maximum	Mean	SD	SE
1960	27	24.54	149.79	56.96	31.08	5.98
2011	27	9.46	130.06	32.96	22.80	4.39
2015	27	15.66	56.09	34.16	10.96	2.11
2017	27	19.23	42.50	30.14	6.77	1.30
2023	27	21.79	52.39	32.27	7.98	1.54

3.5. Vegetation and Vertical Morphological Change Results

The channel bottom profiles, bank heights, and bank angles were identified and mapped at the reach scale. The results can be found in the longitudinal analysis results subsection. Only the active channel bottoms and channel centerlines are reported in this paper. The generated 3D point clouds were used for a point-to-point comparison between the 21 September 2021 and 8 April 2023 UAV flights. The conditions of the concrete and dry walls as confinements were also evaluated during the analysis (Figure 7). The failed confined were marked and saved as a point layer.

The canopy height model (CHM) was obtained with Pix4DMapper using the UAV imagery. The common alder trees found along the channel border ranged in size from 1 m to 15 m in height. Trees of heaven were also spotted as the highest trees along the stream channel. Most of the hanging branches found over the banks were belong to the alder trees. The floodplains were cultivated with tea and hazelnut gardens by the local villagers. The hazelnut trees reached 3–5 m in height. The blackberry plants were found on the banks and along the tributaries entering the study area. The ferns were almost everywhere within the study area. The abandoned bars were vegetated with ferns, blackberries, bushes, alder, willow, and small bushy vegetation.
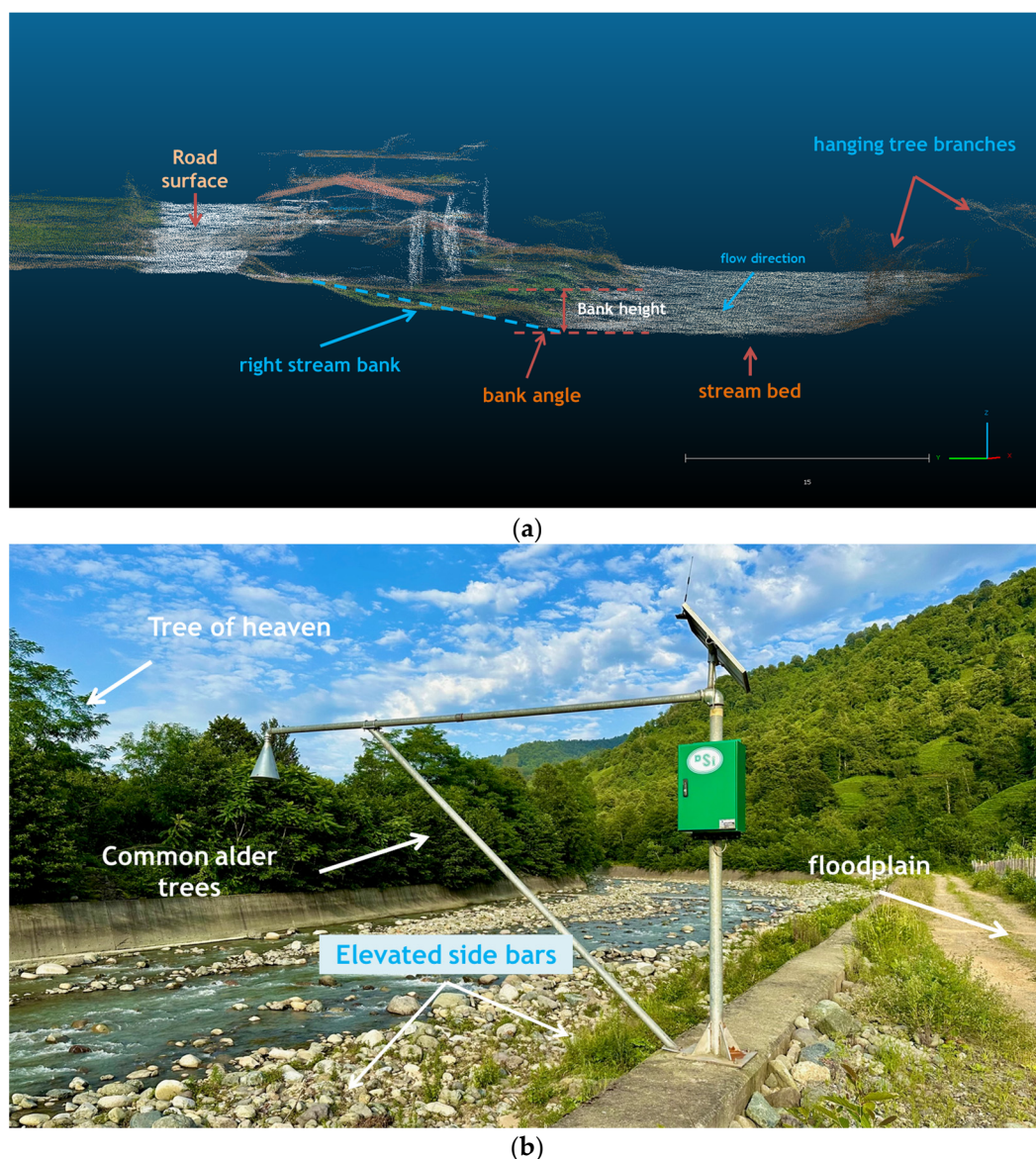
(**a**)

(**b**)

Figure 7. (**a**) The vertical morphological change analysis shows 3D cloud points in great detail on the stream channel bottom and houses built on the stream banks in Senkoy Reach. The image was created from 3D cloud points using CloudCompare software. (**b**) The riparian vegetation, elevated side bars, and floodplain along the stream channel can be seen in the image. The instrument in front is part of a flood warning system operated by the State Hydraulic Works Department.

3.6. Sensitivity Analysis Results

Tables 8 and 9 show the findings of the sensitivity analysis on the overall migration distances and active channel widths. Starting at 10 m, the distance between transects grew at intervals of 25 m. The channel migration lengths were constant up to a transect spacing of 100 m, at which point they started to decline in the 1960–2011 and 2011–2015 timeframes at 150 and 200 m spacings. In the years 2015–2017 and 2017–2023, the declining trend began at spacings of 75 m and 150 m, respectively.

Similar patterns were seen when the active channel widths were measured (Table 9). In the 1960–2011 and 2011–2015 periods, the spacing effect began at a transect spacing of 100 m. The periods of 2015–2017 and 2017–2023 had a stronger influence (Table 9).

Based on the outcomes of the one-way ANOVA test, these changes were not statistically significant at the 0.05 significance level. As a result, the channel distance measurements in this investigation did not experience any spacing effects (Table 10).

Table 8. Sensitivity analysis of the channel migration distances from 1960 to 2023 based on the cross-section measurements for Senkoy Reach.

Number of Transects	Transect Spacing	Channel Migration Distances (m)			
		1960–2011	2011–2015	2015–2017	2017–2023
276	10	24.68	14.89	7.28	6.25
111	25	24.52	14.72	7.94	6.14
55	50	24.98	15.14	6.72	6.08
37	75	24.06	15.36	7.13	5.97
27	100	24.63	15.84	6.19	6.19
18	150	22.67	14.41	6.96	6.34
13	200	19.41	14.41	3.14	5.24

Table 9. Sensitivity analysis of the active channel widths from 1960 to 2023 based on the cross-section measurements for Senkoy Reach.

Number of Transects	Transect Spacing (m)	Active Channel Width (m)				
		1960	2011	2015	2017	2023
281	10	56.04	32.14	33.17	30.39	33.05
111	25	56.25	32.34	33.55	30.72	33.28
55	50	56.44	32.53	33.95	30.85	33.12
37	75	54.53	31.09	32.74	30.87	32.83
27	100	56.96	32.96	34.16	30.14	32.27
18	150	54.17	31.27	36.09	31.86	33.08
13	200	56.66	29.21	33.77	28.64	31.39

Table 10. The one-way ANOVA test results of the channel migration distances from 1960 to 2023 based on the cross-section measurements for Senkoy Reach for the sensitivity analysis.

	Period	Sum of Squares	df	Mean Square	F	Sig.
	Between groups	4.248×10^6	6	707,965.427	0.219	0.971
1960–2011	Within groups	1.716×10^9	531	3,231,272.974		
	Total	1.720×10^9	537			
	Between groups	4.556×10^5	6	75,940.900	0.037	1.000
2011–2015	Within groups	1.082×10^9	531	2,037,723.852		
	Total	1.082×10^9	537			
	Between groups	3.182×10^6	6	530,380.242	0.840	0.540
2015–2017	Within groups	3.354×10^8	531	631,671.312		
	Total	3.386×10^8	537			
	Between groups	1.930×10^6	6	32,167.912	0.104	0.996
2017–2023	Within groups	1.643×10^8	531	309,387.026		
	Total	1.645×10^8	537			

3.7. Field Ground-Truthing Results

The results of the UAV survey and the actual field measurements of the active channel widths are shown in Table 11. The deviations ranged from 0.02 to 4.82 m. The biggest variation in transect number 23 was mostly caused by the plant cover on the transect's left side. The paired comparison analysis test findings revealed that there was a strong correlation (r = 0.972) between the similarity of the two measures. The test findings showed that at the 0.05 level of significance, the active channel widths from the UAV survey and the field measurements were identical ($p = 0.117 > 0.05$).

Table 11. The active channel width measurement results for the ground-truthing for 13 sampled cross-section transects within Senkoy Reach.

	Sampled Cross-Section Transect Numbers												
	27	**23**	**22**	**21**	**18**	**17**	**16**	**15**	**14**	**13**	**10**	**8**	**6**
Active Channel widths (UAV) (m)	44.90	36.58	29.98	22.66	30.48	41.61	28.72	30.12	35.18	28.10	35.32	23.21	21.79
Active Channel widths (field) (m)	43.80	41.40	30.00	24.00	32.00	40.00	30.20	31.00	36.40	30.10	34.82	23.92	21.10
Differences (m)	−1.10	4.82	0.02	1.34	1.52	−1.61	1.48	0.88	1.22	2.00	−0.50	0.71	−0.69

4. Discussion

The lateral channel morphological changes were mostly affected by factors such as channel confinement, channel slope, and sinuosity index (SI) [8,14]. The channel bed deposition and incision were affected by the channel slope, channel bed type (alluvial, semialluvial, or bedrock), and flow volume [7,8,11,74]. Any quarry activities and channel widening distribute suspended sediments to the streams. These results accounted for the majority of channel modifications. The stream channel longitudinal profiles in this study indicated that the channel bottoms fluctuated over 63 years. The 59.38% average decrease in the slope from 1960 to 2023 could be attributed to reaching a confinement ratio of 42% for the left banks and 39% for the right banks. Righini et al. [8] found that in confined and partially confined sub-reaches, the main governing variables were lateral confinement and unit stream power. Their results showed from 1.1 to 6.2 times the pre-flood width and the channel width increased within specific subreaches. There was a noticeable trend toward channel widening, particularly in alluvial subreaches, where the narrowest channels were more likely to increase than the widest channels. Our results show that the channel widening was 43.35% larger than before the confinement construction began.

In our study site, the man-made confinements were begun after 2015 and gradually increased after that. Sholtes et al. [14] reported that the confinement ratio of the active channel bottom width to the bankfull width is a very important predictor of channel widening. Their findings showed that the relationship between channel confinement and flood response existed. They believed that the confined reaches create their own hazards. They found that high–risk fluvial habitats exist in steep, confined reaches as a result of channel incision, hillslope mass wasting, and channel edge erosion. In our study area, many mass concrete confinement walls had collapsed due to an incising stream bed at the meandering channel boundaries. These resulted in exposing the weak banks to the rapid stream flow at the narrowed stream channels (Figure 8).
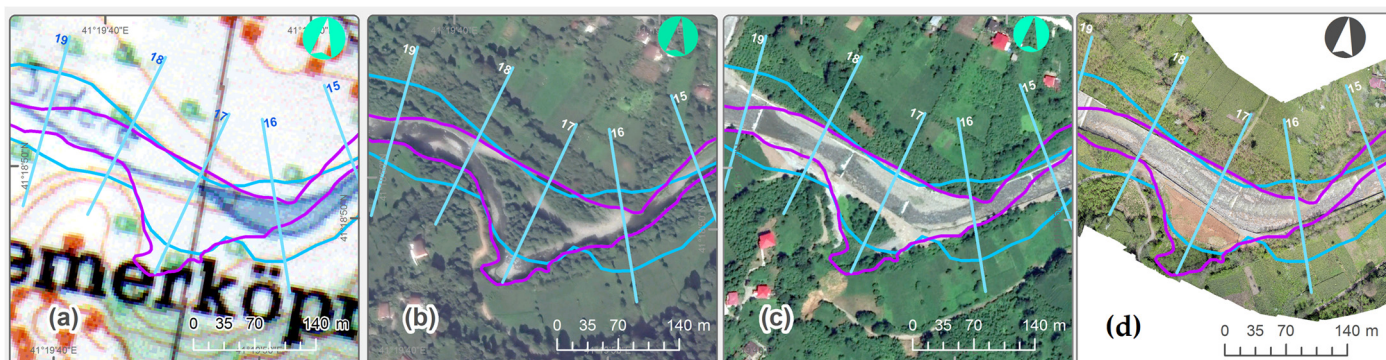

Figure 8. A detailed look at cross-section 17, which is where the lateral channel migration was maximized: (**a**) 1960 toposheet, (**b**) 2011 Google Earth image, (**c**) 2017 Google Earth image, and (**d**) 2023 UAV orthomosaic.

The active channel boundary width shift ranged from 149.79 m to 9.46 m, with an average width shift of 37.3 m over 63 years. A study conducted by Jana [28] in the middle-lower course of the Subarnarekha River, India, showed that the stream active channel boundary shifts were 2.98 m/year for the left banks and 1.84 m/year for the right banks. They found that the shifting increased with the active channel narrowing.

The confinement ratio increase in our study area not only affected the banks but also incised the stream channel bottoms. The 59.38% average slope decrease from 1960 to 2023 indicated the vertical morphological change on the active stream channel bottoms (Figure 9). This can be also attributable to advances in creating more precise DTMs using UAVs. Precise mapping of the stream channel bottoms and creating finer resolution DTMs from the UAV imagery helped to obtain these results in our study area.
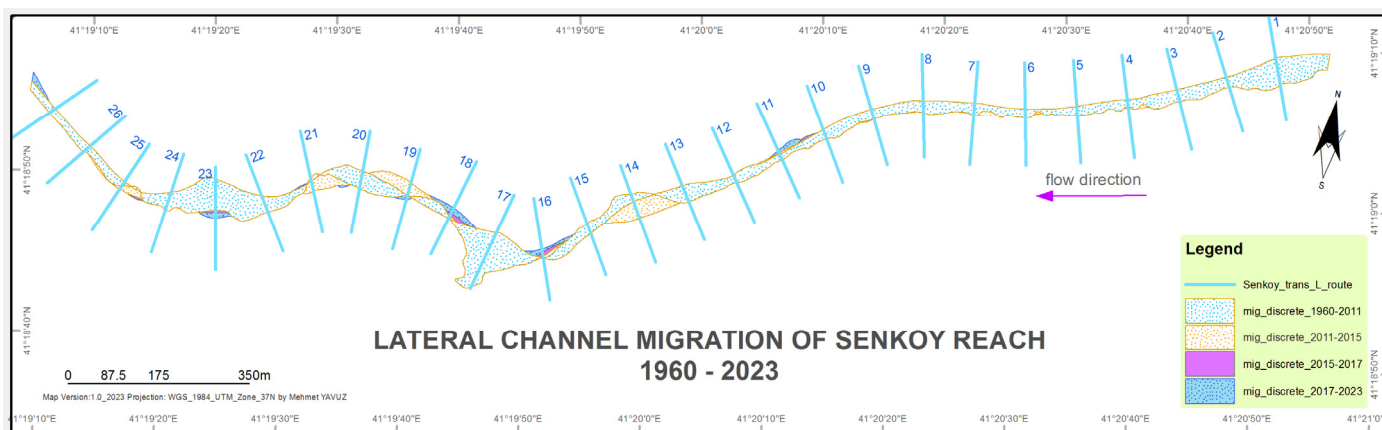
Figure 9. The lateral channel migration from 1960 to 2023 in Senkoy Reach within the Arhavi River Watershed (Türkiye). The shaded areas represent the discrete migration region from 1960 to 2011 (light blue), 2015 (orange), 2017 (magenta), and 2023 (blue) stream channel centerlines. The cross-section ID numbers increase along the flow direction.

One problem of channel mitigation and landform studies is co-registration errors of remotely sensed imagery. Lea and Legleiter [52] believed that the RMSE is simple and a spatially variable (SV) geometric error is more robust than RMSE. The SV error was utilized as an SV level of detection (LoD) to assess the effect of such an error on the quantification of lateral migration. This method enabled the identification of 33% of statistically significant changes (migrations), as opposed to just 24% with the RMSE/uniform error method [52]. An extensive evaluation by Donovan et al. [75] came to the same conclusion: they recommended the generalization of SV error assessment and also recognized the possible necessity for testing SV-LoD on novel metrics of lateral migration, including areal metrics of surface change. We applied second-order polynomial transformation, which gave the lowest RMSE of 22 GCPs when co-registering one topo map and four aerial photographs. This study supported the findings of Lea and Legleiter [52] and Hughes et al. [55]. The third-polynomial transformation gave higher RMSE values than the second-order transformation on our one topo map and four aerial photographs, which gave the same results that Hughes et al. [55] and Lea and Legleiter [52,55] found. The use of small UAVs brought the lateral accuracy to the 2–5 cm level. The results of our analysis demonstrated that the Senkoy Reach orthomosaic's lateral accuracy (XY RMSE) was 1.18 m, which is an acceptable level using 22 GCPs.

The findings of the sensitivity analysis show that, up to a gap of 100 m, the spacing effect on the cross-section transects had no statistically significant impact on measuring active channel width and channel migration distances. Glenn et al. [73] found similar results to ours in research they conducted on the Snake River, which is a big river system in a bedrock confined channel (two 5 km reaches) in King Hill, ID, USA, and on Bear Valley Creek, which is a small river system in an alluvial valley (with 3 km and 1.4 km

long reaches) near Bruce Meadow Airstrip, ID, USA. They revealed that the DEM accuracy was not influenced by the transect spacing when either equally spaced or morphologically spaced. They also reported that differences between the mean depth and the surface areas were negligible. Their findings show that regardless of river size and morphological complexity, transect spacing is the main factor that impacts bathymetry accuracy, whereas methods for finding transects and interpolation are less important [73]. Our 100 m transect spacing is in line with Samuels's [71] suggestion, which is less than 10 times the channel width, and Nanson and Hickin's [68] suggestion, which is less than the meander wavelength.

The use of the UAV for the cross-section survey was found to be very effective based on the field measurements for the ground-truthing and the pairwise comparison analysis. We found that the two datasets were highly correlated (r = 0.972). The paired sample *t*-test results revealed that the two datasets were identical ($p = 0.117 > 0.05$) at the 0.05 significance level. The vegetation cover along the stream's zone made it difficult to measure the transects. The 4.82 m active channel width difference at the 23rd transect could be attributed to the vegetation cover blocking the laser signals. Junaid et al. [34] had similar issues while surveying the rock stability with the UAV. They reported that the vegetation on the rock surface decreases the UAV survey efficiency. The intensity of the vegetation along the stream's riparian zone almost quadrupled compared with the rock surface vegetation (Figure 10a–d). In order to overcome this issue, we surveyed the study area with the UAV during the leaf-off season (21 September 2021 and 9 April 2023). When Gkiatas et al. [38] used the UAV to measure erosion rates on the stream banks of a Mediterranean torrent in Drama, Greece, they discovered findings that were similar to our own. They were able to cover more ground with the UAV than with the conventional erosion pin approach. Furthermore, they demonstrated that the UAV recorded and gathered more measurement points than a conventional GPS survey.
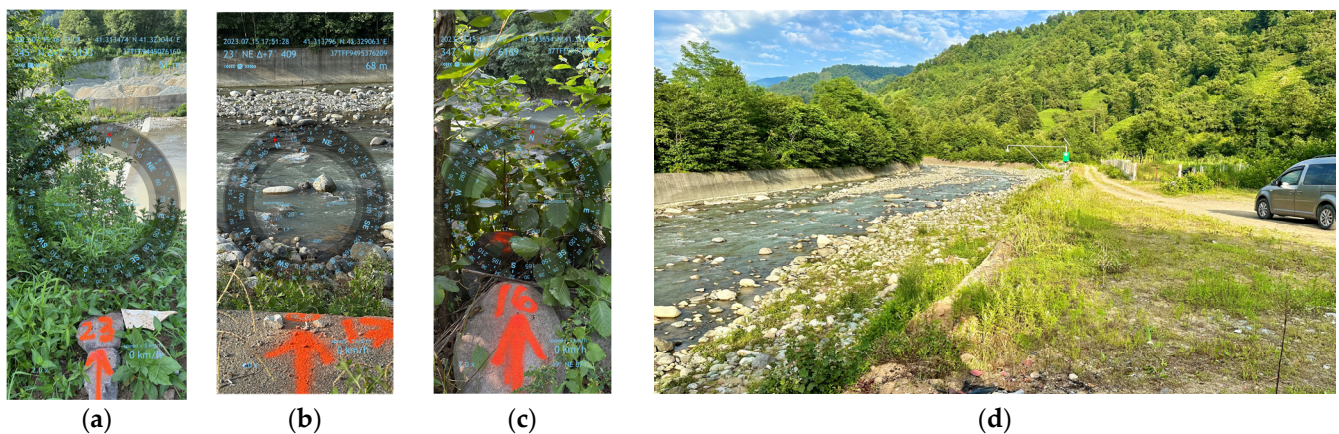

Figure 10. The cross-section transect conditions during the field measurements (**a**) transect 23 with partial vegetation cover, (**b**) an open cross-section transect 17 with no obstruction and the concrete confinement walls can easily be seen, (**c**) the cross-section transect 16 with heavy vegetation obstruction, and (**d**) a part of Sidere Creek and its floodplain on the right. The alluvial bars can be seen within the streams. Photos were captured by Mehmet Yavuz during the field measurements.

Working with a 2785 m long stream reach segment is not common among researchers. The suggested stream length was 12 times the reach width [4,10,76]. Our active channel width and migration analysis showed that working with small UAVs before determining the channel length helped to catch morphological changes at the reach scale at any point. Dunne et al. [69] reported that the role of sediment transport shapes the lateral and vertical change of the active channel morphology. Nanson and Hickin [68] and Hickin and Nanson [67] demonstrated how migration can be extremely discontinuous along a single reach, both in terms of time and distance. It is challenging to infer long-term migration rates from short-term measurements because bends might stay fixed

for tens of years. Our observations after the major flood events on 22 July 2021 in our study area support Dunne et al.'s [69] findings. The sediment transported by the flood event raised the river bed and let the flood water into the Arhavi city streets. It cost over USD 50 thousand in property damage and cleanup efforts to the city of Arhavi, Türkiye [77]. The illegal dumping of dirt and rubble into streams compromises the sediment regime in a riverine ecosystem [33]. These activities can be found at many locations in Senkoy Reach (Figure 11). These illegal activities can be monitored and then effectively and precisely prevented using small UAVs, which can also be used for collecting spatial ecohydrologic and sediment related information [33,43,45,78] at very fine resolutions.

(**a**)   (**b**)

Figure 11. Illegal dumping of (**a**) dirt and rubble into Sidere Creek next to the roads and (**b**) a perspective view of a lower part of the study area. The images were captured by the DJI Air 2S drone.

5. Conclusions

In riverine ecosystems, the hydraulic erosivity of the flood events, the erodibility of the floodplain, the channel along valley edges, and the equilibrium between upstream local sediment supply and the stream's transport capacity must all be closely monitored to mediate these processes. In this study, we used innovative techniques, such as a UAV survey and the Pix4DMapper structure-from-motion (SfM) program, to assess and measure the active channel widening (lateral changes), slope, confinement, sinuosity (longitudinal), deposition, and incision (vertical) changes at the reach scale from 1960 to 2023, along with the historical data. The results of the active channel morphological change factors were compared across 63 years. The following conclusions were drawn from our study:

(1) The channel widening continuously occurred in small amounts (2.98 m/year in the left banks and 1.84 m/year in the right banks) and was maximized during major storm events.

(2) Over 63 years, the channel confinement rose on the left banks from 2.4% to 42% and on the right banks from 5.9% to 34.8%. At the confinement sites, whether natural or man-made, no active channel widening was observed during the field visits.

(3) The CloudCompare analysis using 3D point cloud data showed escalated bars and deposited sediments on the stream beds near the confined banks. These vertical changes—i.e., an increase in the stream bed and a decrease in the wall's height—have raised concerns about protecting the stream banks against stream power, especially during major storm events at meander sites.

(4) The active channel widths measured with the UAV and the TruPulse 360 laser rangefinder were highly correlated (r = 0.972) and identical (p = 0.117 > 0.05) at the 0.05 significance level.

(5) We showcased the fact that the UAV survey offered the same level of accuracy that LiDAR surveying provides with the following benefits: a lower cost, more frequent,

at any time of day, in any season, and with less investment compared with traditional methods.

(6) The UAV survey was found to be an efficient, quick, non-destructive, and multi-temporal way to precisely measure and track the longitudinal, lateral, and vertical morphological changes of a stream channel with great accuracy, even through woody stream channels.

References

1. Walsh, S.J.; Butler, D.R.; Malanson, G.P. An overview of scale, pattern, process relationships in geomorphology: A remote sensing and GIS perspective. *Geomorphology* **1998**, *21*, 183–205.
2. Casado, A.; Peiry, J.-L.; Campo, A.M. Geomorphic and vegetation changes in a meandering dryland river regulated by a large dam, Sauce Grande River, Argentina. *Geomorphology* **2016**, *268*, 21–34.
3. Tufekcioglu, M.; Isenhart, T.M.; Schultz, R.C.; Bear, D.A.; Kovar, J.; Russell, J. Stream bank erosion as a source of sediment and phosphorus in grazed pastures of the Rathbun Lake Watershed in southern Iowa, United States. *J. Soil Water Conserv.* **2012**, *67*, 545–555.
4. Tooth, S. Downstream changes in dryland river channels: The Northern Plains of arid central Australia. *Geomorphology* **2000**, *34*, 33–54.
5. Tufekcioglu, M.; Schultz, R.C.; Isenhart, T.M.; Kovar, J.L.; Russell, J.R. Riparian land-use, stream morphology and streambank erosion within grazed pastures in Southern Iowa, USA: A catchment-wide perspective. *Sustainability* **2020**, *12*, 6461.
6. Rivas Casado, M.; Ballesteros Gonzalez, R.; Kriechbaumer, T.; Veal, A. Automated identification of river hydromorphological features using UAV high resolution aerial imagery. *Sensors* **2015**, *15*, 27969–27989.
7. Bizzi, S.; Lerner, D.N. The use of stream power as an indicator of channel sensitivity to erosion and deposition processes. *River Res. Appl.* **2015**, *31*, 16–27.
8. Righini, M.; Surian, N.; Wohl, E.; Marchi, L.; Comiti, F.; Amponsah, W.; Borga, M. Geomorphic response to an extreme flood in two Mediterranean rivers (northeastern Sardinia, Italy): Analysis of controlling factors. *Geomorphology* **2017**, *290*, 184–199.
9. Pellegrini, G.; Rainato, R.; Martini, L.; Picco, L. The Morphological Evolution of a Step–Pool Stream after an Exceptional Flood and Subsequent Ordinary Flow Conditions. *Water* **2021**, *13*, 3630.
10. Tan, C.; Feng, S.; Zhao, X.; Shan, X.; Feng, S. Longitudinal variations in channel morphology of an ephemeral stream from upland to lowland, Daihai Lake basin, North China. *Geomorphology* **2021**, *372*, 107450.
11. Bollati, I.M.; Pellegrini, L.; Rinaldi, M.; Duci, G.; Pelfini, M. Reach-scale morphological adjustments and stages of channel evolution: The case of the Trebbia River (northern Italy). *Geomorphology* **2014**, *221*, 176–186.
12. Heitmuller, F.T.; Hudson, P.F.; Asquith, W.H. Lithologic and hydrologic controls of mixed alluvial–bedrock channels in flood-prone fluvial systems: Bankfull and macrochannels in the Llano River watershed, Central Texas, USA. *Geomorphology* **2015**, *232*, 1–19.
13. Woellner, R.; Wagner, T.C. Saving species, time and money: Application of unmanned aerial vehicles (UAVs) for monitoring of an endangered alpine river specialist in a small nature reserve. *Biol. Conserv.* **2019**, *233*, 162–175.

14. Sholtes, J.S.; Yochum, S.E.; Scott, J.A.; Bledsoe, B.P. Longitudinal variability of geomorphic response to floods. *Earth Surf. Process. Landf.* **2018**, *43*, 3099–3113.

15. Nanson, G.; Croke, J. A genetic classification of floodplains. *Geomorphology* **1992**, *4*, 459–486.

16. Eker, R.; Aydın, A.; Hübl, J. Unmanned aerial vehicle (UAV)-based monitoring of a landslide: Gallenzerkogel landslide (Ybbs-Lower Austria) case study. *Environ. Monit. Assess.* **2017**, *190*, 28.

17. Šilhán, K. Dendrogeomorphology of different landslide types: A review. *Forests* **2021**, *12*, 261.

18. Yavuz, M.; Koutalakis, P.; Diaconu, D.C.; Gkiatas, G.; Zaimes, G.N.; Tufekcioglu, M.; Marinescu, M. Identification of Streamside Landslides with the Use of Unmanned Aerial Vehicles (UAVs) in Greece, Romania, and Turkey. *Remote Sens.* **2023**, *15*, 1006.

19. Lauer, W.J.; Echterling, C.; Lenhart, C.; Belmont, P.; Rausch, R. Air-photo based change in channel width in the Minnesota River basin: Modes of adjustment and implications for sediment budget. *Geomorphology* **2017**, *297*, 170–184.

20. Maddock, I. The importance of physical habitat assessment for evaluating river health. *Freshw. Biol.* **1999**, *41*, 373–391.

21. Newson, M.D.; Large, A.R. Natural rivers, hydromorphological quality and river restoration: A challenging new agenda for applied fluvial geomorphology. *Earth Surf. Process. Landf. J. Br. Geomorphol. Res. Group* **2006**, *31*, 1606–1624.

22. Akay, S.S.; Özcan, O.; Şanlı, F.B. Quantification and visualization of flood-induced morphological changes in meander structures by UAV-based monitoring. *Eng. Sci. Technol. Int. J.* **2022**, *27*, 101016.

23. Spiekermann, R.; Betts, H.; Dymond, J.; Basher, L. Volumetric measurement of river bank erosion from sequential historical aerial photography. *Geomorphology* **2017**, *296*, 193–208.

24. Janes, V.; Holman, I.; Birkinshaw, S.; O'Donnell, G.; Kilsby, C. Improving bank erosion modelling at catchment scale by incorporating temporal and spatial variability. *Earth Surf. Process. Landf.* **2018**, *43*, 124–133.

25. Tsiakos, C.-A.D.; Chalkias, C. Use of Machine Learning and Remote Sensing Techniques for Shoreline Monitoring: A Review of Recent Literature. *Appl. Sci.* **2023**, *13*, 3268.

26. Lawler, D.M. The measurement of river bank erosion and lateral channel change: A review. *Earth Surf. Process. Landf.* **1993**, *18*, 777–821.

27. Miall, A.D.; Strasser, A. Standards for publications in the field of basin analysis in Earth-science reviews. *Earth Sci. Rev.* **2018**, *177*, 1.

28. Jana, S. An automated approach in estimation and prediction of riverbank shifting for flood-prone middle-lower course of the Subarnarekha river, India. *Int. J. River Basin Manag.* **2021**, *19*, 359–377.

29. Lallias-Tacon, S.; Liébault, F.; Piégay, H. Use of airborne LiDAR and historical aerial photos for characterising the history of braided river floodplain morphology and vegetation responses. *Catena* **2017**, *149*, 742–759.

30. Dewan, A.; Corner, R.; Saleem, A.; Rahman, M.M.; Haider, M.R.; Rahman, M.M.; Sarker, M.H. Assessing channel changes of the Ganges-Padma River system in Bangladesh using Landsat and hydrological data. *Geomorphology* **2017**, *276*, 257–279.

31. Abate, M.; Nyssen, J.; Steenhuis, T.S.; Moges, M.M.; Tilahun, S.A.; Enku, T.; Adgo, E. Morphological changes of Gumara River channel over 50 years, upper Blue Nile basin, Ethiopia. *J. Hydrol.* **2015**, *525*, 152–164.

32. Bao, Y.; Su, L.; Chen, J.; Ouyang, C.; Yang, T.; Lei, Z.; Li, Z. Dynamic process of a high-level landslide blocking river event in a deep valley area based on FDEM-SPH coupling approach. *Eng. Geol.* **2023**, *319*, 107108.

33. Dimitriou, E.; Stavroulaki, E. Assessment of riverine morphology and habitat regime using unmanned aerial vehicles in a Mediterranean environment. *Pure Appl. Geophys.* **2018**, *175*, 3247–3261.

34. Junaid, M.; Abdullah, R.A.; Sa'ari, R.; Rehman, H.; Shah, K.S.; Ullah, R.; Alel, M.N.A.; Zainal, I.Z.; Zainuddin, N.E. Quantification of Rock Mass Condition Based on Fracture Frequency Using Unmanned Aerial Vehicle Survey for Slope Stability Assessment. *J. Indian Soc. Remote Sens.* **2022**, *50*, 2041–2054.

35. Kuhn, J.; Casas-Mulet, R.; Pander, J.; Geist, J. Assessing stream thermal heterogeneity and cold-water patches from UAV-based imagery: A matter of classification methods and metrics. *Remote Sens.* **2021**, *13*, 1379.

36. Brunier, G.; Oiry, S.; Lachaussée, N.; Barillé, L.; Le Fouest, V.; Méléder, V. A Machine-Learning Approach to Intertidal Mudflat Mapping Combining Multispectral Reflectance and Geomorphology from UAV-Based Monitoring. *Remote Sens.* **2022**, *14*, 5857.

37. Diaconu, D.C.; Koutalakis, P.D.; Gkiatas, G.T.; Dascalu, G.V.; Zaimes, G.N. River Sand and Gravel Mining Monitoring Using Remote Sensing and UAVs. *Sustainability* **2023**, *15*, 1944.

38. Gkiatas, G.T.; Koutalakis, P.D.; Kasapidis, I.K.; Iakovoglou, V.; Zaimes, G.N. Monitoring and Quantifying the Fluvio-Geomorphological Changes in a Torrent Channel Using Images from Unmanned Aerial Vehicles. *Hydrology* **2022**, *9*, 184.

39. Rachmawati, T.S.N.; Park, H.C.; Kim, S. A Scenario-Based Simulation Model for Earthwork Cost Management Using Unmanned Aerial Vehicle Technology. *Sustainability* **2023**, *15*, 503.

40. Zhang, X.; Zhu, C.; He, M.; Dong, M.; Zhang, G.; Zhang, F. Failure mechanism and long short-term memory neural network model for landslide risk prediction. *Remote Sens.* **2021**, *14*, 166.

41. Rosgen, D.L. A Practical Method of Computing Streambank Erosion Rate. In Proceedings of the Seventh Federal Interagency Sedimentation Conference, Reno, NV, USA, 25–29 March 2001; pp. 9–15.

42. Hooke, J. An Analysis of the Processes of River Bank Erosion. *J. Hydrol.* **1979**, *42*, 39–62.

43. Duró, G.; Crosato, A.; Kleinhans, M.; Uijttewaal, W. Bank erosion processes measured with UAV-SfM along complex banklines of a straight mid-sized river reach. *Earth Surf. Dyn.* **2018**, *6*, 933–953.

44. Leyland, J.; Hackney, C.R.; Darby, S.E.; Parsons, D.R.; Best, J.L.; Nicholas, A.P.; Aalto, R.; Lague, D. Extreme flood-driven fluvial bank erosion and sediment loads: Direct process measurements using integrated Mobile Laser Scanning (MLS) and hydro-acoustic techniques. *Earth Surf. Process. Landf.* **2017**, *42*, 334–346.

45. Telling, J.; Lyda, A.; Hartzell, P.; Glennie, C. Review of Earth science research using terrestrial laser scanning. *Earth-Sci. Rev.* **2017**, *169*, 35–68.

46. Balestrieri, E.; Daponte, P.; De Vito, L.; Lamonaca, F. Sensors and measurements for unmanned systems: An overview. *Sensors* **2021**, *21*, 1518.

47. Lejot, J.; Delacourt, C.; Piégay, H.; Fournier, T.; Trémélo, M.L.; Allemand, P. Very high spatial resolution imagery for channel bathymetry and topography from an unmanned mapping controlled platform. *Earth Surf. Process. Landf. J. Br. Geomorphol. Res. Group* **2007**, *32*, 1705–1725.

48. Javernick, L.; Brasington, J.; Caruso, B. Modeling the topography of shallow braided rivers using Structure-from-Motion photogrammetry. *Geomorphology* **2014**, *213*, 166–182.

49. Williams, R.; Brasington, J.; Vericat, D.; Hicks, D. Hyperscale terrain modelling of braided rivers: Fusing mobile terrestrial laser scanning and optical bathymetric mapping. *Earth Surf. Process. Landf.* **2014**, *39*, 167–183.

50. Stott, E.; Williams, R.D.; Hoey, T.B. Ground control point distribution for accurate kilometre-scale topographic mapping using an RTK-GNSS unmanned aerial vehicle and SfM photogrammetry. *Drones* **2020**, *4*, 55.

51. Stecca, G.; Zolezzi, G.; Hicks, D.M.; Surian, N. Reduced braiding of rivers in human-modified landscapes: Converging trajectories and diversity of causes. *Earth-Sci. Rev.* **2019**, *188*, 291–311.

52. Lea, D.M.; Legleiter, C.J. Refining measurements of lateral channel movement from image time series by quantifying spatial variations in registration error. *Geomorphology* **2016**, *258*, 11–20.

53. Jaud, M.; Bertin, S.; Beauverger, M.; Augereau, E.; Delacourt, C. RTK GNSS-assisted terrestrial SfM photogrammetry without GCP: Application to coastal morphodynamics monitoring. *Remote Sens.* **2020**, *12*, 1889.

54. Taddia, Y.; Stecchi, F.; Pellegrinelli, A. Coastal mapping using DJI Phantom 4 RTK in post-processing kinematic mode. *Drones* **2020**, *4*, 9.

55. Hughes, M.L.; McDowell, P.F.; Marcus, W.A. Accuracy assessment of georectified aerial photographs: Implications for measuring lateral channel movement in a GIS. *Geomorphology* **2006**, *74*, 1–16.

56. Church, M. Channel morphology and typology. *Rivers Handb.* **1992**, *1*, 126–143.

57. Lourenço, P.; Teodoro, A.C.; Gonçalves, J.A.; Honrado, J.P.; Cunha, M.; Sillero, N. Assessing the performance of different OBIA software approaches for mapping invasive alien plants along roads with remote sensing data. *Int. J. Appl. Earth Obs. Geoinf.* **2021**, *95*, 102263.

58. Wohl, E. Legacy effects on sediments in river corridors. *Earth-Sci. Rev.* **2015**, *147*, 30–53.

59. Rabus, B.; Eineder, M.; Roth, A.; Bamler, R. The shuttle radar topography mission—A new class of digital elevation models acquired by spaceborne radar. *ISPRS J. Photogramm. Remote Sens.* **2003**, *57*, 241–262.

60. Roth, A.; Knopfle, W.; Strunz, G.; Lehner, M.; Reinartz, P. Towards a global elevation product: Combination of multi-source digital elevation models. *Int. Arch. Photogramm. Remote Sens. Spat. Inf. Sci.* **2002**, *34*, 675–679.

61. Karney, C. GeoidEval Utility. Available online: https://geographiclib.sourceforge.io/cgi-bin/GeoidEval (accessed on 5 May 2023).

62. Olson, P.L.; Legg, N.T.; Abbe, T.B.; Reinhart, M.A.; Radloff, J.K. *A Methodology for Delineating Planning-Level Channel Migration Zones*; Washington State Department: Washington, DC, USA, 2014.

63. Rapp, C.F.; Abbe, T.B. *A Framework for Delineating Channel Migration Zones*; Washington State Department of Ecology, Olympia, WA, USA, 2003.

64. Legg, N.T.; Olson, P.L. *Channel Migration Processes and Patterns in Western Washington: A Synthesis for Floodplain Management and Restoration*; Shorelands and Environmental Assistance Program, Washington State Department: Washington, DC, USA, 2014.

65. Legg, N.; Heimburg, C.; Collins, B.; Olson, P. *The Channel Migration Toolbox: ArcGIS Tools for Measuring Stream Channel Migration*; 14-06-032; Department of Ecology State of Washington: Bellevue, WA, USA, 2014; p. 21.

66. Hooke, J.M. Changes in Meander Morphology, International Geomorphology, 1986. In Proceedings of the First International Conference on Geomorphology, Manchester, UK, 15–21 September 1985; John Wiley & Sons: Chichester, UK, 1987; pp. 591–609.

67. Hickin, E.J.; Nanson, G.C. The character of channel migration on the Beatton River, northeast British Columbia, Canada. *Geol. Soc. Am. Bull.* **1975**, *86*, 487–494.

68. Nanson, G.C.; Hickin, E.J. A statistical analysis of bank erosion and channel migration in western Canada. *Geol. Soc. Am. Bull.* **1986**, *97*, 497–504.

69. Dunne, T.; Constantine, J.A.; Singer, M. The Role of Sediment Transport and Sediment Supply in the Evolution of River Channel and Floodplain Complexit. *Trans. Jpn. Geomorphol. Union* **2010**, *31*, 155–170.

70. CloudCompare. *CloudCompare V.2.6.1*; CloudCompare: Dublin, Ireland, 2023.

71. Samuels, P. Cross Section Location in One-Dimensional Models. In Proceedings of the International Conference on River Flood Hydraulics, Wallingford, England, 17–20 September 1990; Wiley: Chichester, UK, 1990; pp. 339–350.

72. Cunge, J.A.; Holly, F.M.; Verwey, A. *Practical Aspects of Computational River Hydraulics*; Pitman Advanced Pub. Program, Boston, MA, USA, 1980.

73. Glenn, J.; Tonina, D.; Morehead, M.D.; Fiedler, F.; Benjankar, R. Effect of transect location, transect spacing and interpolation methods on river bathymetry accuracy. *Earth Surf. Process. Landf.* **2016**, *41*, 1185–1198.

74. Schismenos, S.; Stevens, G.J.; Georgeou, N.; Emmanouloudis, D.; Shrestha, S.; Thapa, B.S.; Gurung, S. Flood and Renewable Energy Humanitarian Engineering Research: Lessons from Aggitis, Greece and Dhuskun, Nepal. *Geosciences* **2022**, *12*, 71.

75. Donovan, M.; Belmont, P.; Notebaert, B.; Coombs, T.; Larson, P.; Souffront, M. Accounting for uncertainty in remotely-sensed measurements of river planform change. *Earth-Sci. Rev.* **2019**, *193*, 220–236.

76. Lemaire, E.; Mreyen, A.-S.; Dufresne, A.; Havenith, H.-B. Analysis of the influence of structural geology on the massive seismic slope failure potential supported by numerical modelling. *Geosciences* **2020**, *10*, 323.

77. Tufekcioglu, M. *Integrated Watershed Management Concept in Flood and Inundation Prevention*; Artvin Coruh University Bulletin: Artvin, Turkey, 2022; pp. 44–48.

78. Valjarević, A.; Algarni, S.; Morar, C.; Grama, V.; Stupariu, M.; Tiba, A.; Lukić, T. The coastal fog and ecological balance for plants in the Jizan region, Saudi Arabia. *Saudi J. Biol. Sci.* **2022**, *30*, 103494.